

CO Reduction

How to cite: *Angew. Chem. Int. Ed.* **2023**, 62, e202214210

International Edition: doi.org/10.1002/anie.202214210

German Edition: doi.org/10.1002/ange.202214210

Surface Water as an Initial Proton Source for the Electrochemical CO Reduction Reaction on Copper Surfaces

Feng Shao^{+,*}, Zhaoming Xia⁺, Futian You⁺, Jun Kit Wong, Qi Hang Low, Hai Xiao^{+,*} and Boon Siang Yeo

Abstract: We have employed in situ electrochemical shell-isolated nanoparticle-enhanced Raman spectroscopy (SHINERS) and density functional theory (DFT) calculations to study the CO reduction reaction (CORR) on Cu single-crystal surfaces under various conditions. Coadsorbed and structure-/potential-dependent surface species, including $^*\text{CO}$, Cu-O_{ad} , and Cu-OH_{ad} , were identified using electrochemical spectroscopy and isotope labeling. The relative abundance of $^*\text{OH}$ follows a “volcano” trend with applied potentials in aqueous solutions, which is yet absent in absolute alcoholic solutions. Combined with DFT calculations, we propose that the surface H_2O can serve as a strong proton donor for the first protonation step in both the C_1 and C_2 pathways of CORR at various applied potentials in alkaline electrolytes, leaving adsorbed $^*\text{OH}$ on the surface. This work provides fresh insights into the initial protonation steps and identity of key interfacial intermediates formed during CORR on Cu surfaces.

intermediates and their initial protonation steps on Cu surfaces can help us gain critical mechanistic insights into the CO_2RR and guide the rational design of more efficient and selective catalysts for desired products.^[2a,3] However, most intermediates generated during the CORR have low coverages and short lifetimes.^[4] In addition, there are other complications from the interplay of surface intermediates, the participation of H_2O solvent, and the local pH/concentration gradients at electrochemical interfaces. These factors render the study of the CORR challenging.^[5]

Shell-isolated nanoparticle-enhanced Raman spectroscopy (SHINERS) is a powerful technique that can provide fingerprint vibrational information of target species on any substrate and material surface with ultrahigh sensitivity (Figure 1a; Figure S1).^[6] The use of SHINERS also overcomes the generality problems of requiring specific materials (plasmonic substrates) and morphologies (nanoscale roughness) for surface-enhanced Raman spectroscopy (SERS). Moreover, SHINERS is particularly applicable to in situ exploration of catalytic processes on single-crystal surfaces with significant sensitivity, stability, and reproducibility.^[7]

Introduction

The electrochemical CO_2 reduction reaction (CO_2RR) is a promising strategy to reduce carbon emissions by directly converting CO_2 into value-added fuels and chemical feedstocks, thereby contributing to a closed-loop carbon cycle.^[1] As a key intermediate in the CO_2RR , the energetics of $^*\text{CO}$ and its further dimerization and protonation determine the selectivity and overpotentials for forming higher-order products.^[2] An in-depth understanding of the CORR

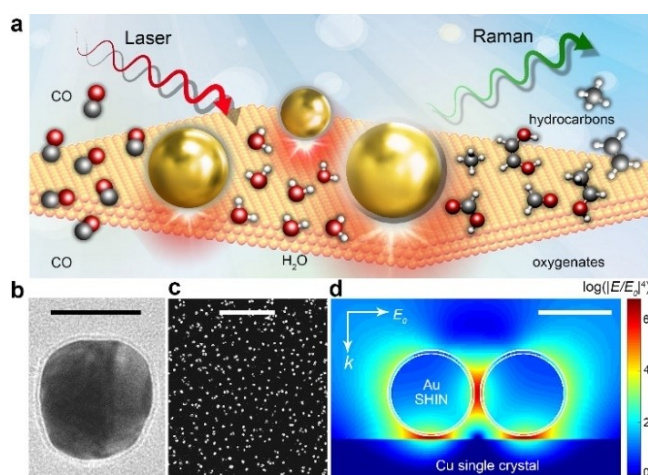


Figure 1. a) In situ EC-SHINERS to study the electrochemical CORR at Cu single-crystal surfaces. b) Transmission electron microscopy (TEM) image of a typical Au@SiO_2 nanoparticle (scale bar: 50 nm). c) Scanning electron microscopy (SEM) image of a $\text{Cu}(100)$ surface modified by Au@SiO_2 SHINs (scale bar: 2 μm). d) Three-dimensional finite-difference time-domain (3D-FDTD) simulations of four SHINs with a 2×2 array on a Cu single-crystal substrate (scale bar: 50 nm). E_z and E_0 denote the localized electric field and the incident electric field under 633 nm laser excitation, respectively; k represents the wavevector of the incident light.

[*] Prof. Dr. F. Shao⁺

State Key Laboratory of Materials-Oriented Chemical Engineering,
 College of Chemical Engineering, Nanjing Tech University
 Nanjing 211816 (China)
 E-mail: feng.shao@njtech.edu.cn

Prof. Dr. F. Shao,⁺ F. You,⁺ J. K. Wong, Dr. Q. H. Low,
 Prof. Dr. B. S. Yeo
 Department of Chemistry, Faculty of Science, National University of
 Singapore
 3 Science Drive 3, Singapore 117543 (Singapore)

Dr. Z. Xia,⁺ Prof. Dr. H. Xiao
 Department of Chemistry, Tsinghua University
 Beijing 100084 (China)
 E-mail: haixiao@tsinghua.edu.cn

[†] These authors contributed equally to this work.

This strategy is achieved by coating a Au nanoparticle core with an ultrathin and pinhole-free SiO₂ shell (≈ 3 nm, Figure 1b; Figure S2). The Au@SiO₂ shell-isolated nanoparticle (SHIN) allows the Au core (≈ 55 nm, Figure 1b) to enhance the electromagnetic field for boosting Raman signals, but prevents it from interfering chemically and electrically with the surroundings.^[6] After drop-casting SHINs onto the Cu electrodes ($\approx 20\%$ coverage, Figure 1c), the junctions between the Au SHINs and Cu surface are known as hotspots (Figure 1d). Raman signal enhancement ($G \propto \log(|E_{\text{sc}}/E|^4)$) within these hotspots is simulated to be more than 10^6 (Figure 1d), thereby facilitating the ultra-sensitive detection of trace adsorbates and intermediates at the electrochemical interfaces (a few nanometers in thickness).^[8]

In this work, we combine electrochemical methods with SHINERS (EC-SHINERS) for in situ monitoring of the CORR on Cu single-crystal electrodes, supported by density functional theory (DFT) calculations. SHINERS spectra of the electrodes were collected in real-time in acidic, neutral, alkaline, and alcoholic electrolytes. Isotope labeling experiments using D₂O and ¹³CO were also carried out. We obtained direct spectroscopic evidence to elucidate the interfacial property and intermediate interaction at the molecular and nanometer scale, which are in line with DFT calculations. The product distribution of the CORR on Cu(100) under various conditions has also been investigated. Our results provide critical mechanistic insights into the hydrogen and oxygen sources for the CORR in alkaline solutions (aqueous and alcoholic), and demonstrate the participation of *H₂O and the formation of *OH in the initial proton transfer of the CORR.

Results and Discussion

In situ EC-SHINERS was first performed on Cu(100) in 0.1 M CsOH electrolyte during the CORR (Figure 2). The copper single-crystal surfaces were prepared and characterized by standard procedures (Figures S3–S5).^[9] Prior to the spectro-electrochemical measurements, surface impurities were removed using a hydrogen evolution reaction (HER) cleaning process (Figures S3–S5).^[10] All reported potentials are referenced to the reversible hydrogen electrode (RHE). The most conspicuous species detected was *CO, identified by its C≡O stretching vibrations at 2060 (on terrace sites) and 2090 cm^{−1} (on step sites), and its C=O stretching vibrations at 1830–1863 cm^{−1} (on bridge sites, Figure S6).^[11] Additionally, we recorded signals at 3400–3480 cm^{−1} that can be attributed to the O–H stretching modes of interfacial H₂O at Cu(100). These bands are potential-dependent since a configurational transition of interfacial H₂O may occur with applied potentials (Figure S6).^[10]

The spectrum of Cu(100) at open circuit potential (OCP, ≈ 0.86 V at pH=13) shows significant peaks around 630 cm^{−1}, which can be assigned to a native Cu₂O layer.^[12] When more negative electrochemical potentials are applied, these Cu₂O signals quickly attenuate, signifying the reduction of the oxide to metallic copper. This observation is

consistent with previous works on Cu₂O electroreduction.^[13] Strikingly, due to sufficient field enhancement from the SHINs, a set of spectral peaks was recorded at around 320 and 400 cm^{−1} from +0.2 V to even −0.8 V (Figure 2a–d). These peaks can be ascribed to the surface Cu oxide phases (Figure S7 and Table S1), and they are explicitly visible under applied potentials as negative as −0.8 V on different Cu surfaces (Figures S8–S14), in line with recent Raman observations.^[7b,14] Furthermore, they are potential-dependent and structure/environment-dependent (Figures S8–S14), implying the general presence and dynamic evolution of the Cu–O_{ad} species and Cu^{δ+} sites on the surfaces during the CORR. Similar results have also been found from operando X-ray techniques and DFT calculations.^[13a,15] Note that, in the absence of the SHINs, no Raman features could be recorded from the bare Cu(100) surface (Figure S15). Furthermore, these surface Cu oxide related peaks (e.g., 320, 400, 630 cm^{−1}) are also invisible in the methanol solution (0.1 M CsOH dissolved in absolute methanol, pH=12.8, Figure 2e; Figure S16).

Another set of peaks grew at about 520 cm^{−1}, and blue-shifted to 543 cm^{−1} with a cathodic scan from +0.2 V to −0.8 V (Figures 2f, g). Remarkably, when the applied potential held at −0.6 V was removed, the peak at 536 cm^{−1} would red-shift back to 520 cm^{−1}, while its intensity attenuated (by 5-fold) and finally disappeared after ca. 60 s (Figure S17), indicating that these Raman peaks are generated from electrochemical processes. According to the DFT results (Figures S18 and S19, and Table S2), we postulate that these bands could belong to the O–H bending modes of the *OH species adsorbed on Cu surfaces interacting with nearby H₂O molecules via hydrogen bonding.^[7b,14] They gradually blue-shift towards the end of the range as the applied potential steps from +0.2 V to −0.8 V (Figure 2g), implying that they are subject to the electrochemical Stark effect with a Stark tuning rate of 20 ± 5 cm^{−1}/V.^[16] Furthermore, a double-peak feature within this region found on Cu(110) is probably due to the *OH species adsorbed at different Cu sites (Figure S8). In particular, this 520–543 cm^{−1} region is absent in the alcoholic solution (Figure 2e; Figure S16) due to the lack of *OH residuals after methanol decomposition and hydrogen formation on Cu surfaces.^[17]

To further verify our assignment for the Cu–OH_{ad} species, EC-SHINERS was performed on Cu(100) in various Ar- and CO-saturated electrolytes with a cathodic (Figure 2b,c) and an anodic scan (Figure S20). Similar peaks were strikingly recorded on Cu(100) in 0.1 M, CO- or Ar-saturated KOH (pH=13.0, Figure S10), LiOH (pH=12.3, Figure S10), CsCl (pH=7.0, Figure S11), and potassium phosphate buffer (PPB, pH=6.0, Figure S12). These observations demonstrate that the 520–543 cm^{−1} peaks cannot possibly originate from the electrolyte anion or from carbon-containing species. We further confirm our assignments by performing ¹³CORR (Figure 2c,f,g). Similar peaks around 521–544 cm^{−1} and dependences of the peak position on applied potential were consistently recorded, which exclude the possibility that the peaks are related to surface Cu–C_{ad} vibrational modes (Figure 2a–d). When replaced

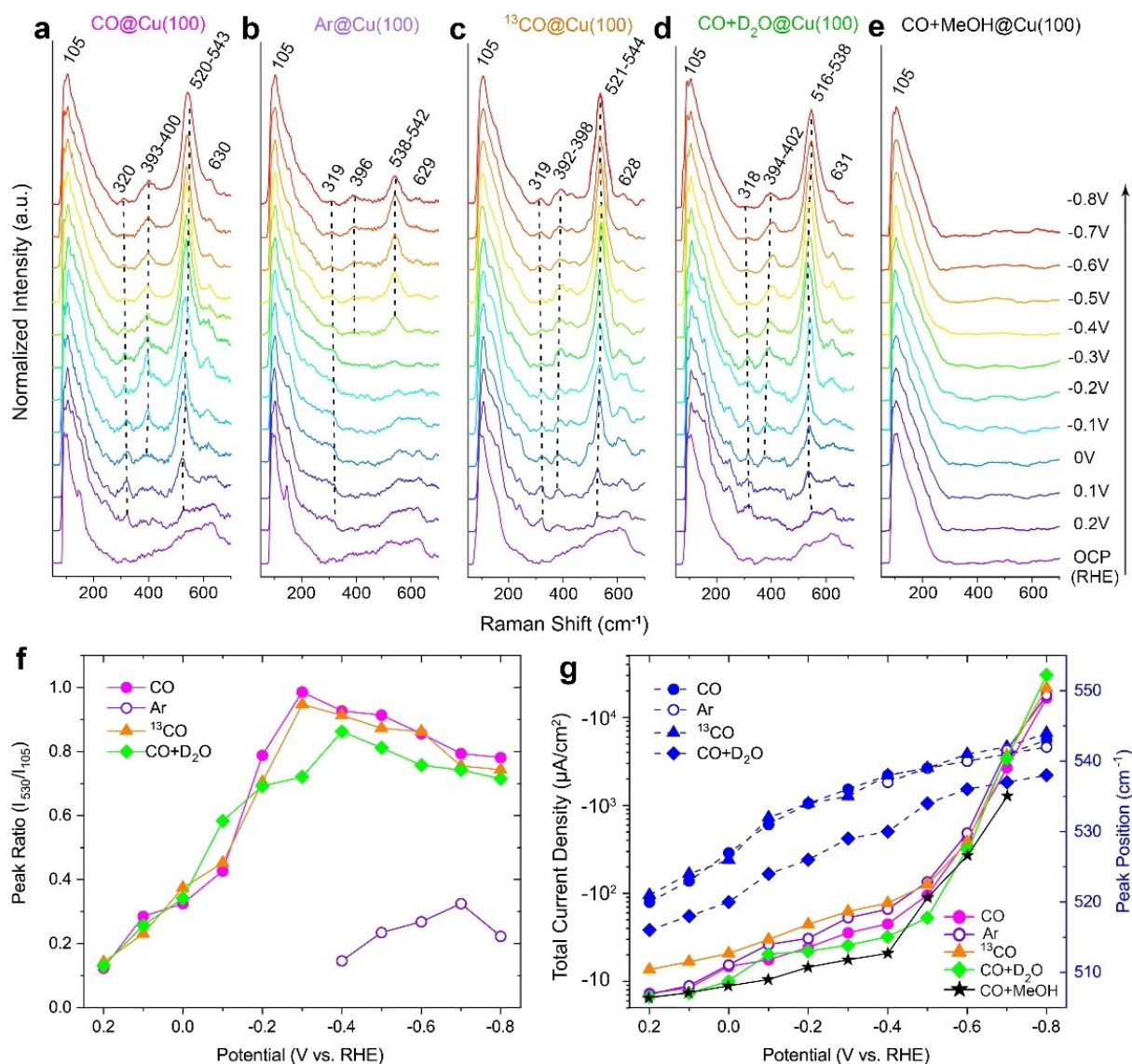


Figure 2. a–e) Normalized EC-SHINERS spectra recorded from the Cu(100) surface in various 0.1 M CsOH/CsOD solutions at different applied potentials (vs. RHE, OCP: open circuit potential). f) Corresponding Raman peak ratios (I_{530}/I_{105}) based on the peak intensities at ≈ 530 cm⁻¹ and 105 cm⁻¹ in various 0.1 M CsOH solutions at different applied potentials. g) The total current densities for the Cu(100) surface and the peak positions around 530 cm⁻¹ in various 0.1 M CsOH solutions at different applied potentials. Key: methanol (MeOH), arbitrary unit (a.u.).

with deuterated water (D₂O) electrolyte (0.1 M CO-saturated CsOD, Figure 2d,f,g), the band range relocates to 516–538 cm⁻¹, where the peak at 538 cm⁻¹ in H₂O red-shifts to 530 cm⁻¹ in D₂O under -0.4 V, hinting that these normal modes involve at least one proton.^[14a] Such a red-shift (8 cm⁻¹) coincides with a recent observation reported by Zhao et al. (7 cm⁻¹ red-shift) for Cu–OH_{ad} species by the D₂O/H₂O isotope exchange,^[14a] yet differs from that by Bodappa et al. (~ 30 cm⁻¹ red-shift).^[7b] This smaller red-shift (8 cm⁻¹) can be attributed to proximally nearer surface Cu–O_{ad} species confining the O–H bending of the *OH in higher alkaline solutions (pH=13).^[14a] All the facts consistently point to the presence of *OH in all the aforementioned systems. We also note these peaks are significantly visible in the spectra recorded from neutral (0.1 M CsCl,

pH=7.0) to acidic (0.1 M PPB, pH=6.0) solutions, indicating that such *OH species could not have been from aqueous OH⁻ ions adsorbed onto the Cu surfaces. Recently, Pfisterer et al. also reported the formation of surface *OH species on Au in sulfuric acid (0.1 M, pH=0.7).^[18]

Peak intensity ratios of the Raman signals at ≈ 530 cm⁻¹ and 105 cm⁻¹ were used to estimate the relative abundance of the surface *OH species (Figure 2f). The low-frequency band at 105 cm⁻¹ is characteristic of the optical fibers used in our spectrometer, and is used as a normalization reference, to compensate for differences in signal intensities due to laser alignment. As the applied potentials become more negative, the I_{530}/I_{105} peak ratios initially rise up to a maximum, then decline moderately, although the turning points are at different potentials. Such a “volcano” trend of

the peak ratios can also be found in different solutions (e.g., H₂O and D₂O, Figure 2f), under different atmospheres (e.g., CO, Ar, and ¹³CO, Figure 2f), and on different facets (e.g., Cu(100), Cu(111), and Cu(110), Figure S8). Notably, compared to Cu(111) and Cu(110), the peak ratios on Cu(100) are always higher under the same applied potentials and similar current densities (Figure 2g; Figures S8 and S9), inferring that the *OH species would be more stable on Cu(100) than the others. This is in accordance with our DFT calculations (Figure S21 and Table S3) and previous computational work.^[19] Moreover, these peak ratios on Cu(100) are also higher in CsOH (Figure 2f) than in KOH and LiOH solutions (Figure S10) under the same conditions. This suggests that larger cations can promote and stabilize *OH species more effectively than smaller cations.^[20]

In contrast to the CO-saturated CsOH (0.1 M) solution, the peak ratios recorded from the corresponding Ar-saturated solution on Cu(100) are much smaller (by ≈ 6.3 -fold), and the *OH bands at 520–543 cm⁻¹ begin at the potential of -0.4 V, while they appeared even at +0.2 V in the CO-saturated solution (Figure 2a,b). However, the observed current densities on each electrolyte follow a similar trend (Figure 2e). This general phenomenon was also observed on the Cu(111), Cu(110), and polycrystalline Cu surfaces, as well as in other different electrolytes (Figures S8–S14). This strongly suggests that the coadsorption of *CO actually strengthens the adsorption of *OH on the Cu single-crystal surfaces at low overpotentials (ca. +0.2 to -0.3 V). However, the *CO/*OH coadsorption is weakened by the hydrogen evolution reaction (HER, ca. -0.4 V) and CO hydrogenation (ca. -0.7 V, Figure 3; Figures S22 and 23), in line with a recent experimental measurement.^[20] All the above observations demonstrate the continued presence of the *OH species on the Cu surfaces during the CORR, challenging a common assumption that the electrochemical CO₂RR primarily occurs on metallic Cu⁰ surfaces, where Cu–OH_{ad} species could not be stable under reductive potentials.^[5a,13a,21] We note that recent in situ EC-STM and

microkinetic modeling results have indicated that *OH/*CO species can coexist on Cu(111) and induce surface reconstruction towards undercoordinated nanostructures at low overpotentials.^[22]

The product distributions of the CORR on Cu(100) were evaluated using chronoamperometry from -0.3 to -0.8 V in different electrolytes (Figure 3; Figures S22 and S23). The Faradaic efficiencies (FEs) and partial current densities of hydrocarbon and oxygenate products are potential-, solvent-, and cation-dependent (Figure 3). For example, at -0.6 V, CO was reduced to a variety of hydrocarbons and oxygenates with different total FEs (C₂₊) in the CsOH aqueous (40.6 %) and methanol (23.7 %) solutions; KOH (38.5 %) and LiOH (32.5 %) aqueous solutions, respectively. In particular, since CsOH is highly soluble both in water and methanol,^[17c,23] significant hydrocarbons (e.g., ethylene and methane) can be formed during the CORR in these two solutions (Figure 3a,b; Figure S22), indicating both water and methanol can act as proton sources for the CORR. Surprisingly, there are no oxygenates formed in the alcoholic solution. According to the isotopically labeled C¹⁸ORR,^[24] this is probably due to the lack of the incorporation of solvent (water) oxygen into oxygenated products (Figure 3b; Figure S22). Additionally, it may also be attributed to no surface *OH formed during the CORR in methanol (Figure 2e),^[17] since the oxygenated products are related to the surface coverage of *OH species, as reported by Duff et al.^[25]

The onset potentials for ethylene (C₂H₄) and methane (CH₄) are found to be ca. -0.3 V and -0.7 V on Cu(100) in alkaline aqueous solutions, respectively, regardless of the cation (Figure 3a,c,d). However, the FEs of C₂H₄ and CH₄ formed, as well as their partial and total current densities (Figure 3; Figures S22 and 23), increase with the size of the cation. These trends are in line with Pérez-Gallent's experimental observations.^[20] Furthermore, the HER starts at ca. -0.4 V for the CsOH aqueous solution, while it turns to more negative potentials at ca. -0.5 V in the KOH and

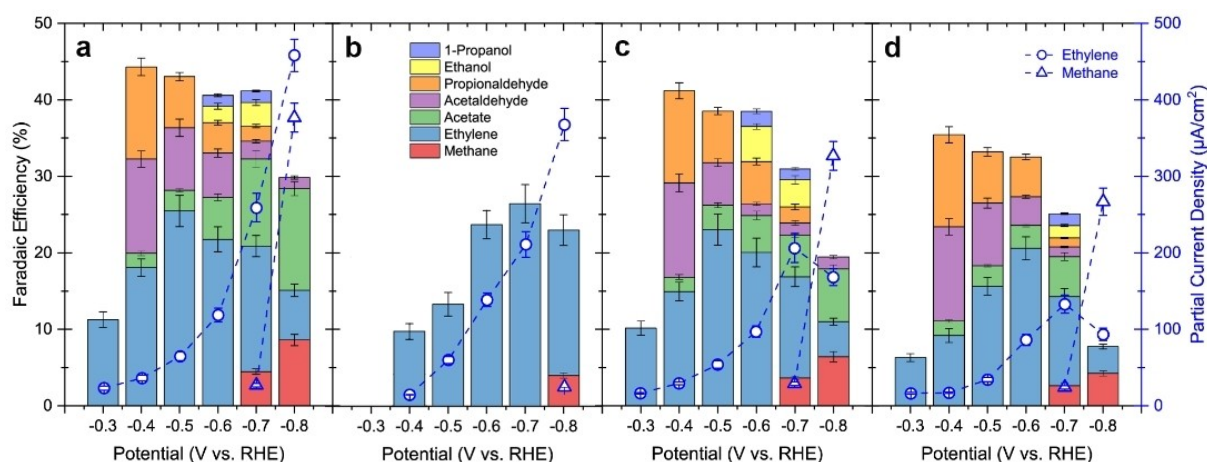


Figure 3. a–d) Faradaic efficiencies and partial current densities of hydrocarbon and oxygenate products during the CORR on Cu(100) in various solutions. a) 0.1 M CsOH (pH = 13.0) aqueous solution; b) 0.1 M CsOH (pH = 12.8) absolute methanol solution; c) 0.1 M KOH (pH = 13.0) and d) LiOH (pH = 12.3) aqueous solutions. The error bars represent the standard deviation from at least three independent measurements.

LiOH solutions (Figure S22). The FEs of H_2 formed decrease with the size of the cation (Figure S22), which can be understood as inhibition of water dissociation and H_2 evolution (the Volmer or Heyrovsky step) by larger cations at the electrified interface in alkaline electrolytes.^[26]

To probe the origin of these *OH species, the “volcano” trend for the peak ratios (I_{530}/I_{105}) in our experiments (Figure 2f), and the initial proton source for the CORR, DFT calculations were further carried out on Cu(100) by taking pH effects and implicit solvation into consideration via a joint methodology, as described in our previous work.^[2a,27] Generally, there are three primary proton sources in aqueous electrolytes: (i) the “hot” water adsorbed on the electrode surface (*H_2O), (ii) the surface hydrogen (*H) generated from the HER, and (iii) the solvated proton (such as H_3O^+).^[2a] In alkaline solutions (pH=13), the solvated proton was excluded, and only the first two proton sources were considered. Combined with the rate-determining steps (RDS) for both the C_1 and C_2 pathways, four possible reaction pathways (1–4) were considered to investigate the initial proton transfer during the CORR (Table 1 and Figure S24).

In our models, the chemical steps occur in pathways 1 and 3. Pathways 2 and 4 involve electrochemical steps (the Volmer steps), which can be affected by the applied pH condition and bias voltage. To model the electrochemical half-cell of pathways 2 and 4, we assumed that these open systems were at dynamic equilibrium with a constantly applied bias potential U , and thus, free energies of electrochemical steps were evaluated through the computational hydrogen electrode (CHE) method.^[2,15b] For a better

comparison, the potentials on the standard hydrogen electrode (SHE) scale in the calculation were converted to that on the RHE scale.

At low overpotentials ($-0.3\text{ V} < U < 0.2\text{ V}$), the coverage of *H on a Cu surface is negligible in alkaline electrolytes (pH=13).^[28] Meanwhile, both pathways 1 or 3 may be thermodynamically activated to produce *OH although it occurs slowly due to a large reaction barrier ($\Delta G^\ddagger = 0.48\text{ eV}$ and 0.49 eV , respectively, Table 1). In this case, only the adsorbed H_2O can serve as the proton source. Note that C_2H_4 formation is allowed at 0.34 V and pH=13, as predicted by a thermodynamic estimation from electrochemical half-reactions (Tables S4 and S5).^[29] As such, we can observe the *OH peak at $\approx 530\text{ cm}^{-1}$ even at 0.2 V in the 0.1 M CsOH solution (Figure 2a), owing to the high sensitivity of the EC-SHINERS technique and high stability of the *OH species at low overpotentials (Table S3).

At the experimental onset potential around -0.3 V , the C_2 products (e.g., C_2H_4) prevail during the CORR (Figure 3; Figure S22). Based on DFT calculations, a single CO adsorbs upright on Cu(100) bridge sites with π^* back-donation dominated chemical bonds, and the O atom in CO is negatively charged ($Q = -1.09|e|$, Figure S25). Thus, when two CO molecules closely adsorb on Cu(100) bridge sites with a C–C distance of 2.98 \AA , the resulting electrostatic repulsion between two CO prevents them from dimerizing to *C_2O_2 , which renders this step to be the RDS for the C_2 pathway in the CORR.^[30] The resulting *C_2O_2 forms strong hydrogen bonding with *H_2O on adjacent Cu sites, with a $O_{\text{dimer}}-H_{\text{water}}$ distance of 1.56 \AA (Figure S26). The charge difference suggests a significant increase in the electron density on the O atoms of *C_2O_2 when close to the H atoms of *H_2O (Figure S26). This indicates that the hydrogen bonds between *C_2O_2 and nearby *H_2O decrease the electrostatic repulsion between two CO to stabilize the dimer. After the CO–CO coupling ($\Delta G^\ddagger = 0.48\text{ eV}$, Table 1), the proton in H_2O^* would be easily transferred to *C_2O_2 , resulting in the *OCCOH and *OH species on the surface spontaneously (pathway 2, Table 1; Figures S27 and S28). This proton transfer process has also been confirmed by ab initio molecular dynamics calculations in our recent work.^[31]

The Volmer step is considered as the first step and RDS of the HER on Cu surfaces at low overpotentials in alkaline electrolytes (pH=13).^[28] Our calculations show that the Volmer step occurs spontaneously in both pathways 2 and 4 under negative potentials (Table 1). Moreover, the reaction free energy of the Volmer step becomes more negative with the decrease of overpotential (Figure S24), and thus the coverage of *H increases accordingly. Prior to the onset potential of the Volmer step (ca. $U = -0.4\text{ V}$, Figure S22), adsorbed H_2O can serve as the proton source for pathways 2 or 4. After the activation of the Volmer step (ca. $-0.7\text{ V} < U < -0.4\text{ V}$), there is competition between the HER and the C_2 pathways of the CORR, and both the surface *H and H_2O^* would serve as proton donors. While the coadsorbed *H could reduce the CO dimerization barrier in pathway 2 ($\Delta G^\ddagger = 0.34\text{ eV}$, Table 1), the dimer’s first protonation suffers from a higher barrier of 0.29 eV using *H as the proton donor than using H_2O^* as the proton source ($\Delta G =$

Table 1: Free energy profiles of reaction pathways for the initial protonation steps during the CORR.^[a]

Pathways	Reactions	ΔG [eV]	ΔG^\ddagger [eV]
1	$4^* + 2CO + 2H_2O \rightarrow 2^*CO + 2H_2O^*$	−1.13	
	$2^*CO \rightarrow ^*C_2O_2$	0.26	0.48
	$(2^*CO \rightarrow ^*C_2O_2)$	(0.10)	(0.34)
	$^*C_2O_2 + H_2O^* \rightarrow ^*OCCOH + ^*OH$	−0.13	
2	$4^* + 2CO + 2H_2O \rightarrow 2^*CO + 2H_2O^*$	−1.13	
	$^* + e^- + H_2O \rightarrow ^*H + OH^-$ (Volmer step)	−0.22	
	$2^*CO \rightarrow ^*C_2O_2$	0.10	0.34
	$^*C_2O_2 + ^*H \rightarrow ^*OCCOH$	0.25	0.29
	$(^*C_2O_2 + H_2O^* \rightarrow ^*OCCOH + ^*OH)$	(−0.13)	
3	$2^* + CO + H_2O \rightarrow ^*CO + H_2O^*$	−0.56	
	$^*CO + H_2O^* \rightarrow ^*COH + ^*OH$	0.49	0.49 ^[b]
4	$^* + CO \rightarrow ^*CO$	−0.71	
	$^* + H_2O + e^- \rightarrow ^*H + OH^-$ (Volmer step)	−0.39	
	$^*CO + ^*H \rightarrow ^*CHO + ^*$	0.65	0.86
	$(^*CO + H_2O^* \rightarrow ^*COH + ^*OH)$	(0.49)	(0.49) ^[b]

[a] ΔG is the overall free energy change from the reactant to the product, and ΔG^\ddagger is the barrier energy change from the transition state (TS) to the reactant. (pH=13, $T=298.15\text{ K}$, $U=-0.34\text{ V}$ vs. RHE). [b] This ΔG^\ddagger is approximated with the ΔG because the TS for this step is very close to the final product both geometrically and energetically. Reaction steps and energy profiles in brackets are possible parallel reactions in different pathways.

−0.13 eV, the fifth step in pathway 2). Accordingly, under such conditions, the surface H_2O^* is still the dominant proton source for dimer protonation (pathway 2, Table 1).

With the bias potential becoming more negative ($U < -0.7$ V), the C_1 pathways (e.g., CH_4 formation with the onset potential at ca. −0.7 V) of the CORR are activated (Figure 3). Compared to forming $^*\text{CHO}$ via reactions between $^*\text{CO}$ and $^*\text{H}$ in pathway 4 ($\Delta G^\ddagger = 0.86$ eV), the initial protonation of CO to $^*\text{COH}$ has a lower barrier of 0.49 eV in pathway 4, suggesting that the H_2O^* also prevails over the proton source for the first CO protonation (Figures S29 and S30). However, for more negative potentials (e.g., $U < -0.8$ V), the Volmer step occurs so fast that the coverage of $^*\text{H}$ will increase rapidly. Most of the surface H_2O would be consumed for the HER, then only the $^*\text{H}$ could serve as the proton source for both the C_1 and C_2 pathways.

Considering only the initial proton transfer at different applied potentials (ca. $-0.8 \text{ V} < U < 0.2 \text{ V}$), both the C_1 and C_2 pathways present a similar phenomenon that the proton transfer from the H_2O^* to the O atom of $^*\text{CO}$ is much easier than that from the $^*\text{H}$ to the C atom (Table 1; Figure S24). When the H_2O^* acts as a proton source, it will leave an $^*\text{OH}$ on the Cu surface after the initial proton transfer (Table 1). With the negative shift of bias potentials (ca. $-0.3 \text{ V} < U < 0.2 \text{ V}$), the overall reaction rate of the CORR can be promoted accordingly, and thus the resulting $^*\text{OH}$ species will accumulate on the Cu surface. After fully activating the Volmer step (ca. $U = -0.4$ V), the $^*\text{H}$ coverage will increase, thereby lowering the $^*\text{CO}$ and $^*\text{OH}$ coverages on the Cu surface. Additionally, more negative bias potentials (ca. $-0.8 \text{ V} < U < -0.4 \text{ V}$) will promote the desorption of $^*\text{OH}$ ($^*\text{OH} + \text{e}^- \rightarrow ^* + \text{OH}^-$), which also suppresses its accumulation. Hence, the peak ratio (I_{530}/I_{105}) curve shows a “volcano” trend in the SHINERS spectra for the $^*\text{OH}$ species (Figure 2f).

Conclusion

In summary, we employed in situ electrochemical SHINERS to probe the interfacial properties and reaction intermediates formed during the CORR on Cu single-crystal surfaces. By systematically comparing spectra recorded on different Cu surfaces and in various electrolytes, we demonstrated that coadsorbed surface species ($\text{Cu}-\text{O}_{\text{ad}}$, $\text{Cu}-\text{OH}_{\text{ad}}$, and $^*\text{CO}$) and their interactions could be directly identified by in situ EC-SHINERS and confirmed by isotopic experiments, suggesting the existence of $\text{Cu}-\text{O}_{\text{ad}}/\text{Cu}-\text{OH}_{\text{ad}}$ species and $\text{Cu}^{\delta+}$ sites even under very negative potentials. Adsorbed $^*\text{CO}$ was found to reinforce $^*\text{OH}$ adsorption to the surface, and this effect was more prominent on $\text{Cu}(100)$ than on $\text{Cu}(111)$ and $\text{Cu}(110)$. The larger cations (e.g., Cs^+) played a more significant role in the stabilization of the $^*\text{OH}$ adsorption and the promotion of C_{2+} products than small cations (e.g., K^+ and Li^+) under the same conditions. The product distribution of oxygenates and hydrocarbons could be regulated by the applied potential, solvent, cation size, and $^*\text{OH}$ species during the CORR on $\text{Cu}(100)$. The relative

abundance of the $^*\text{OH}$ species (i.e., the I_{530}/I_{105} peak ratios) showed a “volcano” trend with a cathodic potential scan. Combined with DFT calculations, we concluded that the surface H_2O^* molecules act as proton donors for both the $^*\text{C}_2\text{O}_2$ and $^*\text{CO}$ protonation, leaving $^*\text{OH}$ species on the Cu surfaces at various potentials (ca. $-0.8 \text{ V} < U < 0.2 \text{ V}$ vs. RHE) in alkaline electrolytes ($\text{pH} = 13$). This work increases our mechanistic understanding of the CO_2 RR at the molecular scale and provides a versatile methodology to study electrocatalytic systems operating under different conditions, including CO oxidation, oxygen reduction reaction, nitrate reduction reaction, and metal corrosion.

Acknowledgements

We thank the State Key Laboratory of Materials-Oriented Chemical Engineering at Nanjing Tech University (Nos. SKL-MCE-22 A01 and 39801178) and the Ministry of Education, Singapore (A-0004135-00-00) for the financial support of this work. Z. X. and H. X. are grateful for the financial support from the National Natural Science Foundation of China (Nos. 22122304 and 21903047). Z. X. is also supported by the China Postdoctoral Science Foundation (2020M680507). The shell-isolated nanoparticles (SHINs) were prepared by Prof. Jian-Feng Li (Xiamen University, China). We thank J.-F. Li. for collecting the TEM image as shown in Figure 1b.

Conflict of Interest

The authors declare no conflict of interest.

Data Availability Statement

The data that support the findings of this study are available in the supplementary material of this article.

Keywords: CO Reduction Reaction • Proton Sources • Single-Crystal Surfaces • Surface Species • In Situ Raman

- [1] a) L. Wang, S. Nitopi, A. B. Wong, J. L. Snider, A. C. Nienlander, C. G. Morales-Guio, M. Orazov, D. C. Higgins, C. Hahn, T. F. Jaramillo, *Nat. Catal.* **2019**, 2, 702–708; b) A. D. Handoko, F. Wei, Jendy, B. S. Yeo, Z. W. Seh, *Nat. Catal.* **2018**, 1, 922–934.
- [2] a) H. Xiao, T. Cheng, W. A. Goddard, *J. Am. Chem. Soc.* **2017**, 139, 130–136; b) J. K. Nørskov, J. Rossmeisl, A. Logadottir, L. Lindqvist, J. R. Kitchin, T. Bligaard, H. Jónsson, *J. Phys. Chem. B* **2004**, 108, 17886–17892.
- [3] a) Y. Zheng, A. Vasileff, X. Zhou, Y. Jiao, M. Jaroniec, S.-Z. Qiao, *J. Am. Chem. Soc.* **2019**, 141, 7646–7659; b) Y. Y. Birdja, E. Pérez-Gallent, M. C. Figueiredo, A. J. Göttle, F. Calle-Vallejo, M. T. M. Koper, *Nat. Energy* **2019**, 4, 732–745.
- [4] J.-C. Dong, X.-G. Zhang, V. Briega-Martos, X. Jin, J. Yang, S. Chen, Z.-L. Yang, D.-Y. Wu, J. M. Feliu, C. T. Williams, Z.-Q. Tian, J.-F. Li, *Nat. Energy* **2019**, 4, 60–67.

- [5] a) K. P. Kuhl, E. R. Cave, D. N. Abram, T. F. Jaramillo, *Energy Environ. Sci.* **2012**, *5*, 7050–7059; b) T. Cheng, H. Xiao, W. A. Goddard, *Proc. Natl. Acad. Sci. USA* **2017**, *114*, 1795–1800; c) H. Xiao, T. Cheng, W. A. Goddard, R. Sundararaman, *J. Am. Chem. Soc.* **2016**, *138*, 483–486; d) K. Jiang, R. B. Sandberg, A. J. Akey, X. Liu, D. C. Bell, J. K. Nørskov, K. Chan, H. Wang, *Nat. Catal.* **2018**, *1*, 111–119.
- [6] a) J. F. Li, Y. F. Huang, Y. Ding, Z. L. Yang, S. B. Li, X. S. Zhou, F. R. Fan, W. Zhang, Z. Y. Zhou, D. Y. Wu, *Nature* **2010**, *464*, 392–395; b) J.-F. Li, Y.-J. Zhang, S.-Y. Ding, R. Panneerselvam, Z.-Q. Tian, *Chem. Rev.* **2017**, *117*, 5002–5069.
- [7] a) C.-Y. Li, J.-C. Dong, X. Jin, S. Chen, R. Panneerselvam, A. V. Rudnev, Z.-L. Yang, J.-F. Li, T. Wandlowski, Z.-Q. Tian, *J. Am. Chem. Soc.* **2015**, *137*, 7648–7651; b) N. Bodappa, M. Su, Y. Zhao, J.-B. Le, W.-M. Yang, P. Radjenovic, J.-C. Dong, J. Cheng, Z.-Q. Tian, J.-F. Li, *J. Am. Chem. Soc.* **2019**, *141*, 12192–12196.
- [8] E. C. Le Ru, E. Blackie, M. Meyer, P. G. Etchegoin, *J. Phys. Chem. C* **2007**, *111*, 13794–13803.
- [9] Y. Huang, A. D. Handoko, P. Hirunsit, B. S. Yeo, *ACS Catal.* **2017**, *7*, 1749–1756.
- [10] C.-Y. Li, J.-B. Le, Y.-H. Wang, S. Chen, Z.-L. Yang, J.-F. Li, J. Cheng, Z.-Q. Tian, *Nat. Mater.* **2019**, *18*, 697–701.
- [11] a) C. M. Gunathunge, X. Li, J. Li, R. P. Hicks, V. J. Ovalle, M. M. Waegle, *J. Phys. Chem. C* **2017**, *121*, 12337–12344; b) A. S. Malkani, M. Dunwell, B. Xu, *ACS Catal.* **2019**, *9*, 474–478; c) P. Hollins, *Surf. Sci. Rep.* **1992**, *16*, 51–94.
- [12] Y. Deng, A. D. Handoko, Y. Du, S. Xi, B. S. Yeo, *ACS Catal.* **2016**, *6*, 2473–2481.
- [13] a) H. Mistry, A. S. Varela, C. S. Bonifacio, I. Zegkinoglou, I. Sinev, Y.-W. Choi, K. Kisslinger, E. A. Stach, J. C. Yang, P. Strasser, B. R. Cuenya, *Nat. Commun.* **2016**, *7*, 12123; b) B. Beverskog, I. Puigdomenech, *J. Electrochem. Soc.* **1997**, *144*, 3476–3483.
- [14] a) Y. Zhao, X. Chang, A. S. Malkani, X. Yang, L. Thompson, F. Jiao, B. Xu, *J. Am. Chem. Soc.* **2020**, *142*, 9735–9743; b) G. Niaura, *Electrochim. Acta* **2000**, *45*, 3507–3519; c) M. Moradzaman, G. Mul, *ChemElectroChem* **2021**, *8*, 1478–1485.
- [15] a) R. M. Arán-Ais, F. Scholten, S. Kunze, R. Rizo, B. Roldan Cuenya, *Nat. Energy* **2020**, *5*, 317–325; b) H. Xiao, W. A. Goddard, T. Cheng, Y. Liu, *Proc. Natl. Acad. Sci. USA* **2017**, *114*, 6685; c) A. Bagger, L. Arnarson, M. H. Hansen, E. Spohr, J. Rossmeisl, *J. Am. Chem. Soc.* **2019**, *141*, 1506–1514.
- [16] I. V. Chernyshova, P. Somasundaran, S. Ponnurangam, *Proc. Natl. Acad. Sci. USA* **2018**, *115*, E9261.
- [17] a) R. García-Muelas, Q. Li, N. López, *ACS Catal.* **2015**, *5*, 1027–1036; b) R. Ben David, A. Ben Yaacov, A. R. Head, B. Eren, *ACS Catal.* **2022**, *12*, 7709–7718; c) S. Kaneco, K. Iiba, N.-H. Hiei, K. Ohta, T. Mizuno, T. Suzuki, *Electrochim. Acta* **1999**, *44*, 4701–4706.
- [18] J. H. K. Pfisterer, F. Nattino, U. E. Zhumaev, M. Breiner, J. M. Feliu, N. Marzari, K. F. Domke, *ACS Catal.* **2020**, *10*, 12716–12726.
- [19] W. J. Durand, A. A. Peterson, F. Studt, F. Abild-Pedersen, J. K. Nørskov, *Surf. Sci.* **2011**, *605*, 1354–1359.
- [20] E. Pérez-Gallent, G. Marcandalli, M. C. Figueiredo, F. Calle-Vallejo, M. T. M. Koper, *J. Am. Chem. Soc.* **2017**, *139*, 16412–16419.
- [21] S. Nitopi, E. Bertheussen, S. B. Scott, X. Liu, A. K. Engstfeld, S. Horch, B. Seger, I. E. Stephens, K. Chan, C. Hahn, *Chem. Rev.* **2019**, *119*, 7610–7672.
- [22] A. Auer, M. Andersen, E.-M. Wernig, N. G. Hörmann, N. Buller, K. Reuter, J. Kunze-Liebhäuser, *Nat. Catal.* **2020**, *3*, 797–803.
- [23] S. Kaneco, K. Iiba, H. Katsumata, T. Suzuki, K. Ohta, *Chem. Eng. J.* **2007**, *128*, 47–50.
- [24] M. Jouny, W. Luc, F. Jiao, *Nat. Catal.* **2018**, *1*, 748–755.
- [25] C. S. Le Duff, M. J. Lawrence, P. Rodriguez, *Angew. Chem. Int. Ed.* **2017**, *56*, 12919–12924; *Angew. Chem.* **2017**, *129*, 13099–13104.
- [26] a) B. Huang, R. R. Rao, S. You, K. Hpone Myint, Y. Song, Y. Wang, W. Ding, L. Giordano, Y. Zhang, T. Wang, S. Muy, Y. Katayama, J. C. Grossman, A. P. Willard, K. Xu, Y. Jiang, Y. Shao-Horn, *JACS Au* **2021**, *1*, 1674–1687; b) M. R. Thorson, K. I. Siil, P. J. Kenis, *J. Electrochem. Soc.* **2013**, *160*, F69.
- [27] T. Cheng, H. Xiao, W. A. Goddard, *J. Phys. Chem. Lett.* **2015**, *6*, 4767–4773.
- [28] a) P. Farinazzo Bergamo Dias Martins, P. Papa Lopes, E. A. Ticianelli, V. R. Stamenkovic, N. M. Markovic, D. Strmcnik, *Electrochem. Commun.* **2019**, *100*, 30–33; b) A. Bagger, R. M. Arán-Ais, J. Halldin Stenlid, E. Campos dos Santos, L. Arnarson, K. Degn Jensen, M. Escudero-Escribano, B. Roldan Cuenya, J. Rossmeisl, *ChemPhysChem* **2019**, *20*, 3096–3105.
- [29] K. P. Kuhl, T. Hatsukade, E. R. Cave, D. N. Abram, J. Kibsgaard, T. F. Jaramillo, *J. Am. Chem. Soc.* **2014**, *136*, 14107–14113.
- [30] a) E. Pérez-Gallent, M. C. Figueiredo, F. Calle-Vallejo, M. T. M. Koper, *Angew. Chem. Int. Ed.* **2017**, *56*, 3621–3624; *Angew. Chem.* **2017**, *129*, 3675–3678.
- [31] F. Shao, J. K. Wong, Q. H. Low, M. Iannuzzi, J. Li, J. Lan, *Proc. Natl. Acad. Sci. USA* **2022**, *119*, E2118166119.

Manuscript received: September 26, 2022

Accepted manuscript online: November 11, 2022

Version of record online: December 8, 2022